Structural Analysis of a Mars Science Helicopter Blade: Lessons Learned

Dorcas V. Kaweesa[1]
Aerospace Engineer
NASA Ames Research Center
Moffett Field, CA, USA

Gianmarco Sahragard-Monfared[2]
Aerospace Engineer
NASA Ames Research Center
Moffett Field, CA, USA,

Joshua Bowman[3]
Research Associate
Science and Technology Corporation
Moffett Field, CA, USA

ABSTRACT

NASA's successful demonstration of powered flight on Mars through the Ingenuity Helicopter, as part of the Mars 2020 Perseverance rover mission, has led to the development of next generation Martian rotorcraft. The future of Martian rotorcraft has evolved to include high payload-carrying vehicles to possibly contribute to planetary science missions, which will require improved flight dynamics and rotor aerodynamic performance to fly at nominally high forward flight speeds and at higher flight altitudes. To ensure the feasibility and viability of successful mission performance, it is also critical to mature the structural design for advanced Martian rotorcraft to bridge the gap between the best practices of the spacecraft and aircraft communities. This paper focuses on the structural analysis of a Mars Science Helicopter (MSH) blade using finite element methods. Multiple loading conditions including launch and operational flight were applied to investigate the blade's structural integrity. The blade's modal natural frequencies were also analyzed to investigate the blade's dynamic behavior.

INTRODUCTION

The groundbreaking success of the Ingenuity helicopter revolutionized powered flight on Mars thereby demonstrating the power of aerial mobility and the capability of future Mars exploration [1]. As a technology demonstrator, Ingenuity provided a baseline for flight heritage on Mars. With a total mass of 1.8kg and no dedicated science payload, Ingenuity demonstrated a flight speed of ~10m/s with original flight specifications of about 90 seconds over a range of 180m [2, 3]. Following Ingenuity's success, the future of Martian and planetary rotorcraft is advancing to contribute to science missions and space-related investigations for which payload-carrying vehicles with long flight range capabilities and higher flight altitudes are envisioned [3, 4, 5, 6]. Several advanced Martian rotorcraft designs have been conceptualized to account for the need for increased payload capability [7, 8, 9]. The Sample Recovery Helicopters (SRH) [10] were Ingenuity-class vehicles proposed to assist in the retrieval of samples as part of NASA's Mars Sample Return mission. The Mars Science Helicopter (MSH) [11, 12] was a larger hexacopter rotorcraft concept developed for independent science missions.

Presented at the Vertical Flight Society's Vertical Lift Aircraft Design & Aeromechanics Specialists' Conference, San Jose, CA, USA, Jan. 27-29, 2026.

The Chopper conceptual vehicle [13, 14] is a hexacopter designed to be capable of 3km per flight while carrying a minimum 3kg payload and builds on the MSH and SRH efforts. These advanced vehicles require new rotor designs, improved rotor aerodynamic performance, improved flight dynamics, controls, and handling qualities, and lightweight structural designs. In addition, they require large enough battery capacity to provide longer range and increased speed in forward flight. Since Ingenuity, notable research has been conducted in areas including flight dynamics [15] for efficient flight control systems and performance optimization, rotor performance [16, 17, 18] for rotor structural and performance predictions, and rotor blade aerodynamic optimization for advanced Martian rotorcraft [19, 20, 21] to computationally and experimentally investigate and improve the aerodynamic efficiency of rotor blades in low Reynolds number regimes like the Martian atmosphere. Table 1 summarizes various rotor parameters for different conceptualized rotorcraft designs compared to Ingenuity.

To understanding the aerodynamic performance of rotorcraft blades, it is important to analyze their structural performance to ensure that the blades meet airworthiness standards for flight in the Martian atmosphere and that rotor blade design and weight are optimized while maintaining structural integrity. This is especially critical for the thin blades designed for the Martian atmosphere, as blade flexibility may yield elastic deformation that may negatively influence aerodynamic performance.

Table 1. Rotor Structure Comparison for Conceptualized Martian Rotorcraft.

Parameters	Ingenuity	MSH	SRH	Chopper
Mass (kg)	1.8	~31	2.5	36.1
Radius (m)	0.605	0.64	0.706	0.675
Thrust-weighted solidity	0.148	0.142	0.128	0.30
Payload	None	5kg	None	3-12

This paper focuses on the structural analysis of rotor blades for the Mars Science Helicopter. Previous work investigated the structural analysis of MSH's load bearing components and the impact of adjusting mass estimates [22]. The MSH rotorcraft was a proposed vehicle concept that would perform science investigations independently of a land-based vehicle. Compared to Ingenuity's coaxial rotor configuration, the MSH concept was a hexacopter (Figure 1) designed to carry dedicated payload for independent science investigations on Mars. As rotorcraft development has shifted from pure technology demonstration to science mission operation and potential assistance for human space exploration, it is critical to mature both the vehicle's structural design and rotor aerodynamic performance

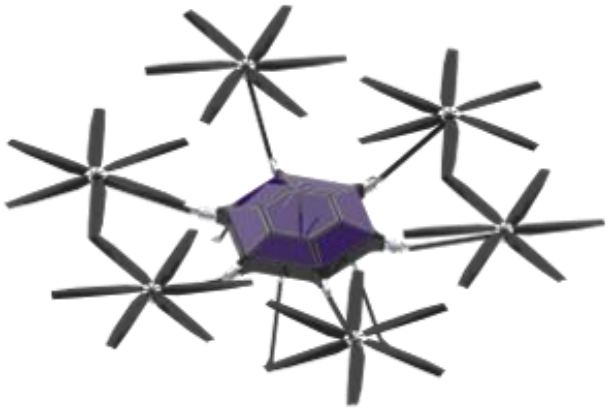

Figure 1. Next-generation conceptual Mars Science Helicopter (MSH) capable of carrying ~5kg of dedicated science payload.

For a nominal vehicle mass of ~31kg, structural analyses performed on the MSH's load bearing components (the rotor arms and frame/fuselage) as presented in Ref. 20 provided insight on the stress and mass estimates of the structure that help guide the selection of materials necessary to achieve an optimal lightweight structure. This was accomplished by determining minimum acceptable component thicknesses that would allow the MSH to survive 26G launch loads and regular operation on Mars. Additionally, the preliminary structural design and aeromechanical design of the MSH baseline rotors has been reported considering unique airfoil geometries [23, 24, 25]. A series of blade analyses were previously performed by University of Maryland considering the same material properties as those used with the Ingenuity blade [25]. The work presented herein reports the structural and vibrational analysis of the MSH blade considering a new set of materials used in blades as manufactured by Sensenich.

APPROACH

The conceptual MSH had six rotors with four blades per rotor for a solidity of 0.142. The complex MSH blade design features thin airfoils with sharp leading and trailing edges, and the airfoil design changes at various radial stations as the blade transitions from root to tip along the blade span (Figure 2). Table 2 summarizes the rotor geometry including the twist and chord of the MSH blade at different radial stations. The structural composition of a single MSH blade is composed of an internal foam structure which is overlaid with the spar. The skin is then overlaid on the outermost surface of the blade stretching from the root to the tip.

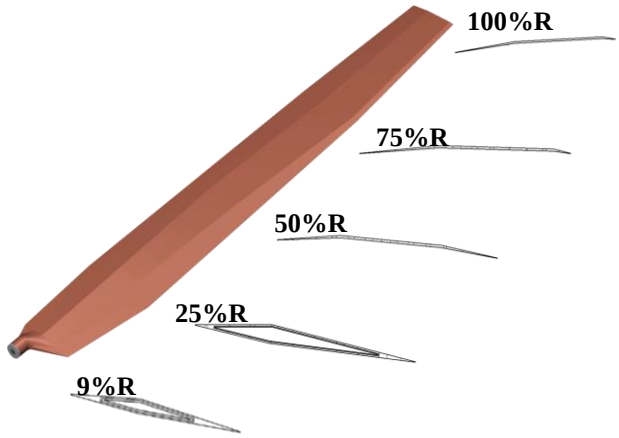

Figure 2. Rendered model of the MSH blade showing airfoil shapes at different radial stations.

Table 2. MSH Blade Geometry.

Radial Station (% r/R)	Chord (m)	Twist (deg)	Thickness to Chord Ratio (t/c)
0.09	0.0605	11.89	8%
0.25	0.0831	9	8%
0.50	0.0799	4.5	1%
0.75	0.0766	0	1%
1	0.0580	-4.5	1%

The goals for the MSH blade structural analysis are to ensure and maintain consistency with the material properties used for forthcoming blade structural analyses and experimental tests and to provide a baseline understanding of the behavior of complex blade fabrications for future Mars or planetary applications. In addition, the MSH blade analysis examined the structural

integrity based on a series of loading conditions. Composite materials were selected for each subcomponent to ensure a lightweight blade structure. These materials are summarized in Table 3 and are detailed in Tables A1 and A2 of Appendix A. Since the spar is the primary load-bearing structure in a blade, unidirectional carbon fiber was selected for the spar to ensure reinforcement and to maintain the blade's structural rigidity. Bidirectional carbon fiber was used in the skin, which aligned the fibers in two directions, offering more flexibility in the complex design. It should be noted that the units were converted to the SI to comply with the units of the blade geometry used in the analysis. Based on the carbon fiber and foam core material properties assigned to the MSH blade, the total blade structural mass is 0.0713kg.

Table 3. Materials for the MSH blade subcomponents.

Blade Component	Material	Mass (kg)
Foam	Rohacell70	0.0016
Skin	Bi-directional carbon fiber	0.0542
Spar	Uni-directional carbon fiber	0.0155

The MSH blade CAD model (Figure 3) was developed in SOLIDWORKS and translated into a .STEP file for readability into Abaqus/CAE software. Abaqus/CAE was used as the finite element analysis tool for the quasistatic stress and non-rotating modal frequency analyses of the blade. The simulation tool has built-in procedures for material property assignment, material orientation, model meshing, and load distribution. The same materials (Table 3) were used in the Abaqus simulations, and two material distributions were compared. Isotropic material distribution was defined by the Young's modulus and Poisson's ratio, assuming uniformity and homogeneity for stiffness and elasticity in any plane of direction of the applied stress. The orthotropic material distribution was defined by Young's modulus, Poisson's ratio, and shear modulus (input as Engineering Constants in Abaqus), assuming directional dependency of the materials. In this case, the material orientation was defined in the x-direction along the blade span.

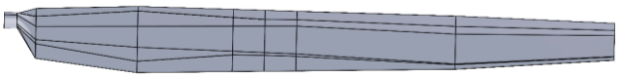

Figure 3. Rendered CAD of the MSH Blade.

The non-rotating modal frequency analysis which simulated the blade in a deployed configuration with the rotor arm assembly extended as shown in Figure 1, examined the blade's structural modes and corresponding natural frequencies. This provided a fundamental understanding of the blade's dynamic characteristics.

For the quasistatic stress analysis of the MSH blade, different loading conditions were considered. First, the Mass Acceleration Curve (MAC) [26] as shown in Figure 4 was used to determine an approximate launch load to be applied to the blade assuming a stowed configuration. Ref. 22 illustrates both stowed and deployed configurations of the MSH conceptual design. Since the MSH blade is lightweight and hardly supported, except at the hub, compared to other MSH structural components, a much higher quasistatic load was expected. As such, a 60G quasistatic load was deemed acceptable to simulate a load experienced during launch based on the single MSH blade's mass, considering smaller components would possibly experience greater acceleration. Next, a 0.3G load was applied to simulate the MSH blade in a deployed configuration during non-rotating operations accounting for Martian gravity. In Abaqus, both 60G and 0.3G quasistatic loads were applied to the entire blade as a gravity load type in the mechanical category.

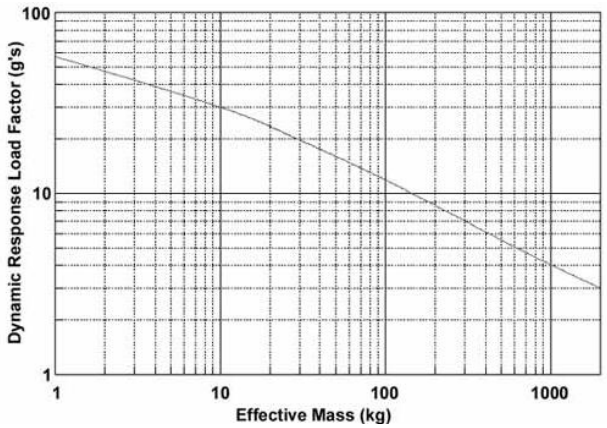

Figure 4. Mass-Acceleration Curve [26].

Additionally, a series of blade loads including centrifugal force, chordwise force, and a normal force were applied to understand the structural limits and determine the structural feasibility of the blade design. The blade loads were obtained in a systematic procedure that involved using the Blade Sectional Properties Generator (BSPGen) tool to calculate sectional elastic, inertial, and geometric properties at discrete radial stations along the span of the MSH blade. BSPGen utilizes elastic beam theory and the weighted composite area method to calculate geometric properties such as elastic axis, inertial properties such as radius of gyration, stiffnesses such as flap stiffness, and the mass distribution along the span of the blade. The required inputs for these calculations are chord normalized airfoils, chord and twist distributions, radius, composite layup schedule, and material properties.

The sectional properties from BSPGen were used as inputs in the Comprehensive Analytical Model of Rotorcraft

Aerodynamics and Dynamics II (CAMRAD II) software tool [27]. In CAMRAD II, a case study was set up for a four-bladed rotor at 0° collective and 2700RPM. Other parameters considered as flight conditions included air density, tip Mach, and flight speed, among others. The blade loads were obtained as forces and moments for various radial stations from 10% to 100% radius along the blade span. In Abaqus, each of the blade loads was applied as a body force along the blade span with the centrifugal force applied axially, the chordwise force applied from the leading edge to the trailing edge, and the normal force applied perpendicular to the top surface of the blade in the local principal axes. An additional case was set with the centrifugal force applied as a rotational body force using an RPM input in terms of angular velocity.

RESULTS

Non-Rotating Modal Frequency Analyses

The goal for performing a non-rotating modal frequency analysis was to primarily understand the dynamic behavior and structural response of the MSH blade. Two separate analyses were run for the same blade with either isotropic or orthotropic distribution of the subcomponents' material properties. The blade's natural frequencies and their corresponding mode shapes were determined for up to 12 modes as presented in Table 4. Mode 1 corresponds to flap or bending frequency, Mode 3 corresponds to a twist effect or a torsional frequency, and Mode 5 corresponds to the lag or chordwise frequency. The other modes were combinations of flap, lag, and torsional modes. The mode shapes revealed the blade's deformation pattern at each frequency. By visualizing the mode shapes, the frequencies at which large deformation and potential failure could occur can be identified. Understanding the mode shapes and related frequencies offers design insight on how to optimize the blade geometry, mass distribution, and stiffness that will change the blade's dynamic characteristics while maintaining an optimal lightweight design with enhanced structural integrity.

Comparing the natural frequency of the blade between isotropic and orthotropic material distribution, the results showed that the blade with the isotropic material model had higher natural frequencies than the orthotropic material model. Although the material's mass density was the same with total blade mass of 0.0713kg, the decrease in the frequency with orthotropic material distribution was due to the inherent dependence on the material's direction. A lower natural frequency indicates lower overall stiffness in that specific mode of vibration. Natural frequencies can be optimized by controlling the direction of the material's distribution. One notable challenge, however, is that natural frequencies vary due to the dependency on the material's direction within the structure, which introduces complexities in dynamic characteristics and response to vibrations especially for complex structures.

Table 4. MSH blade natural frequencies and mode shapes.

Mode	Frequency (Hz) Isotropic	Frequency (Hz) Orthotropic	Mode Shape
1	19.331	15.352	1st flap
2	60.814	39.192	Coupled mode
3	118.96	74.823	1st torsion
4	151.10	104.44	Coupled mode
5	199.22	118.51	1st lag
6	258.36	142.10	2nd torsion
7	346.72	203.65	Coupled mode
8	422.23	245.17	3rd torsion
9	532.23	280.80	Coupled mode
10	603.27	355.62	4th torsion
11	691.24	423.65	Coupled mode
12	750.03	470.89	5th torsion

Quasistatic Stress Analyses

The first set of analyses examined the peak stresses of the blade when subjected to a 60G load to simulate a launch load and a 0.3G load accounting for Martian gravity. It is important to note that since the MSH blade is not geometrically linear, nonlinear effects for large deformation and displacements were accounted for in Abaqus. Peak stresses were examined for the skin, spar, and foam core separately since each subcomponent contributes to identifying the optimal structural behavior and possible regions of failure within the blade. Table 5 presents the peak stresses for each of the blade subcomponents.

Table 5. Peak stresses of the MSH blade subcomponents due to 60G and 0.3G loads.

	Peak Stress (MPa) Isotropic		Peak Stress (MPa) Orthotropic	
Blade Component	60G load	0.3G load	60G load	0.3G load
Skin	538.57	1.49	719.12	3.72
Spar	567.97	2.97	758.29	4.11
Foam core	1.35	0.0069	2.92	0.0155

The spar experienced the highest stress due to the concentrated strength in a single direction based on the unidirectional carbon fiber material assigned. Results

showed a peak stress based on a 60G launch load was ~568MPa considering an isotropic material distribution, whereas the peak stress for an orthotropic material distribution was approximately ~758MPa. Recall that according to the mass acceleration curve (Figure 4), structural mass will dictate the allowable dynamic response load factor (g's). For a 0.3G load simulating Martian gravity, the blade's peak stresses in the spar were much lower; 3.75MPa and 4.11MPa for the isotropic and orthotropic material distributions respectively. Figure 5 and Figure 6 show the stress distribution in the blade when subjected to 60G and 0.3G loading, respectively. The peak stress regions in the spar (Figure 7) are areas of high stress concentration because of geometric discontinuities in the spar. Stress concentrations should be minimized to reduce the likelihood of failure in the blade and ensure the blade's durability.

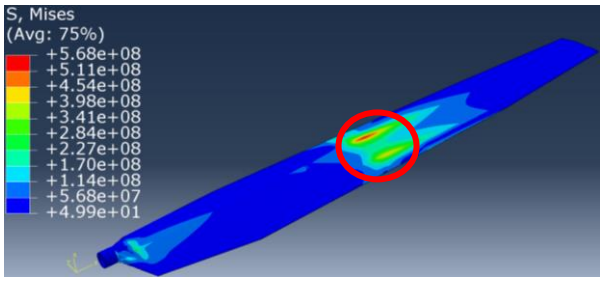

Figure 5. Stress distribution in the MSH blade based on 60G loading.

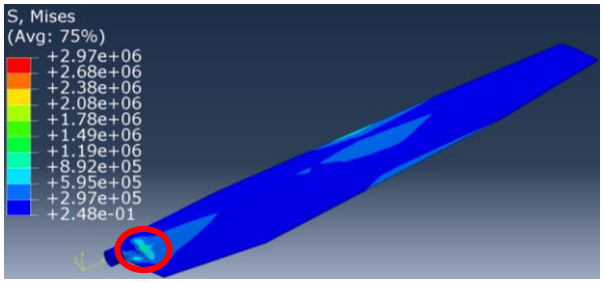

Figure 6. Stress distribution in the MSH blade based on 0.3G loading.

Based on the ultimate stress of the unidirectional carbon fiber (~1.54GPa) in the spar and the bidirectional carbon fiber (~868MPa) in the skin, the safety factors (FoS >1) for both the 60G and 0.3G loading cases lie within the allowable limit for the material properties of the carbon fiber defined implying safer structures. Note that for launch loads, a safety factor of 1 is satisfactory while for operational loads, a safety factor >3 is satisfactory.

Furthermore, isotropic material distribution offers predictable structural response resulting in uniform stress distribution compared to orthotropic distribution which varies along different directions. Due to the blade design with varying chord, twist, and the orthotropic distribution of the carbon fiber material, the blade will likely experience non-uniform failure, especially at uneven and sharp interfaces. Peak stress did not occur on the outer surface, the skin, but likely in an interior surface. This depended on the material orientation, ply stacking, and the loading conditions. As such, it is imperative that high-strength materials including carbon fiber are directionally optimized and aligned with the anticipated direction of primary stresses to allow for strong, lightweight structures.

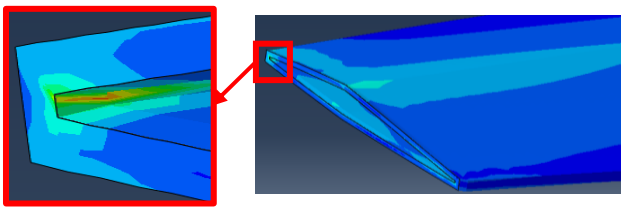

Figure 7. Cross section of the blade showing region of peak stress in the interior layer of the blade spar.

Blade Loads Analysis

Following the preliminary analysis of the blade based on 60G and 0.3G loading conditions, three separate cases were set up in Abaqus to analyze the impact of individual blade loads (axial, chordwise, and normal forces) on the MSH blade. The detailed results of the blade forces from CAMRAD II are presented in Table A3 in Appendix A. These analyses examined the response of the MSH blade under specified loading to understand the structural limits and determine the structural feasibility of the blade. Due to computational limitations and potential convergence difficulties, nonlinear effects were not accounted for in Abaqus.

In Abaqus/CAE, three separate finite element models of the same MSH blade were set up for each blade loading condition. Based on the mean forces obtained for the different radial stations from CAMRAD II, analytical mathematical expressions were derived and input in Abaqus to define the respective magnitude and load distribution. The coordinate system of the MSH blade used in the finite element analyses considered the positive x-direction along the blade span from root to tip, and as shown in Figure 8, a reference point was added as center of rotation (CoR) to factor in the distance from the actual blade to the center of the hub and account for a 0.64m rotor radius. Another reference point was added to the blade root portion to which a fixed boundary condition was applied to the root end of the blade to restrict any rotation and translation.

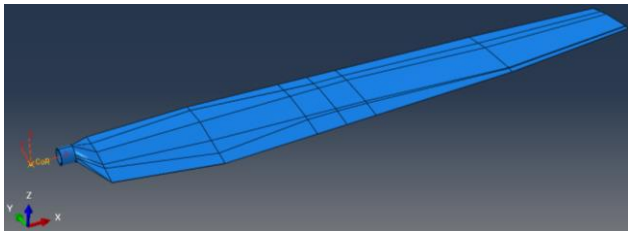

Figure 8. Coordinate system of the MSH blade showing the center of rotation.

Following the coordinate system of the blade model with the x-direction along the blade span, an analytical mathematical expression for the mean axial forces was obtained. The axial forces used were generated from CAMRAD II for different radial stations as presented in the fifth column of Table A3 in Appendix A. The axial force, also referred to as the centrifugal force, was assigned in Abaqus, as a distributed body force and applied as a loading per unit volume over the entire blade (Figure 9). Distributing the axial force as a body force in Abaqus caused linear acceleration throughout the volume of the blade. This analysis simulated quasistatic centrifugal effects to determine the peak stresses and the impact of a centrifugal force on the blade as the primary driver of structural stress.

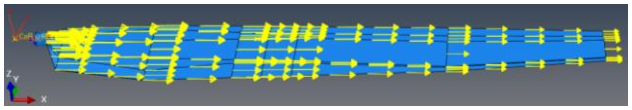

Figure 9. MSH blade model showing the axial force applied along the blade span.

Results from the blade's analysis were examined for the skin, spar, and foam separately and showed that there were higher stresses in the skin (Table 6). The comparison between the isotropic and orthotropic material distribution of the carbon fiber provided an understanding of how material orientation may impact the structural behavior. In this case, orthotropic distribution of the carbon fiber yielded stresses that were higher than each of the material's ultimate stress, indicating that the blade design could have experience an overload and could not withstand the applied force. Stresses were predominantly localized near the blade root in the skin, spar and foam as shown in Figure 10.

These regions likely had high stress concentrations due to the blade's geometric discontinuities and complex non-linearity and could lead to structural failure. Considering the zero collective setting, the blade generated zero aerodynamic lift, however the steady centrifugal force acted as a constant force pulling the blade outward from the hub, thereby contributing to the overall structural stress of the blade, particularly at the root.

Table 6. Peak stresses of the blade subcomponents subjected to an axial force.

Blade Component	Peak Stress (GPa) Isotropic	Peak Stress (GPa) Orthotropic
Skin	2237.49	3419.00
Spar	942.22	2525.60
Foam	3.17	7.85

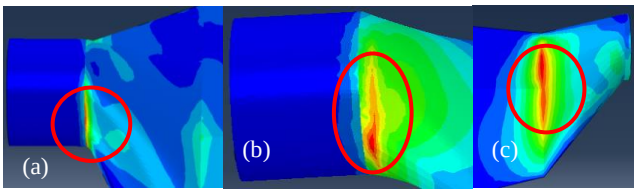

Figure 10. FEA of blade showing regions of peak stress on the (a) skin; (b) spar; and (c) foam due to an axial force.

In an additional simulation, a different procedure was implemented in Abaqus by assigning the centrifugal force as a rotational body force with an angular velocity of 282.74 radians/second, which is equivalent to 2700RPM. The goal was to analyze and compare centrifugal loading effects based on two different load simulation approaches. The centrifugal force in this case was governed by the mathematical expression in Equation 1 where ω is the angular velocity, r is the distance between any point to the axis of rotation considering different radial stations, and $\rho(x)$ is the mass per unit length of the blade (kg/m).

$$F = \int_r^R \omega^2 \rho(x) dx \qquad (1)$$

As part of the procedure, the rotational body force was applied to simulate loads from rotation by defining the axis of rotation (two points) and a magnitude in terms of angular velocity away from the axis of rotation. The load set up is shown in Figure 11. Though the hub is not included in the model set up, a reference point referred to as CoR was added to define the position of the hub and the center of rotation. This turning effect caused angular acceleration simulating the blade rotating around a fixed axis. A fixed boundary.

The peak stress of the blade due to a 282.74 radians/second rotational body force was also observed in the skin. The peak stresses for each blade component, which mostly occurred near the blade root, are presented in Table 7. These areas of high stress concentration can make the blade susceptible to structural failure. Comparing the results from both approaches, that is applying a body force to the blade as opposed to a rotational body force at approximately 2700RPM, the stresses experienced in all blade subcomponents exceeded the actual ultimate stress

for the bidirectional carbon fiber (UTS = ~868MPa), the unidirectional carbon fiber (UTS = ~1.54GPa), and the Rohacell70 (UTS = 2.2MPa). This implied that the safety factors based on the prescribed loading conditions did not lie within the allowable limits of the material properties assigned. The difference in magnitude of the stresses from either approach can be credited to the nature of the applied force in terms of the force's magnitude and direction. The angular velocity applied in the rotational body force approach assumed a uniform mass density over the total length of the blade. This is subject to change if the material properties or blade geometry is adjusted for different use cases thereby impacting the blade's structural behavior.

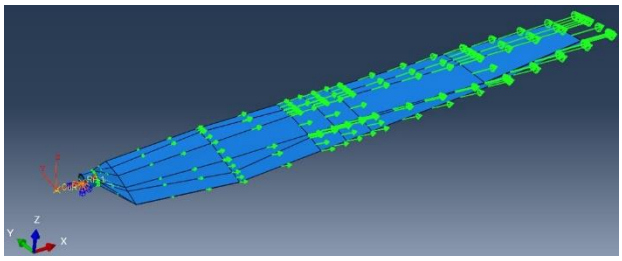

Figure 11. Rotational body force applied to the blade with the center of rotation (CoR) shown offset from the blade root.

Table 7. Peak stresses of the blade under centrifugal effects via a rotational body force.

Blade Component	Peak Stress (GPa) Isotropic	Peak Stress (GPa) Orthotropic
Skin	33.20	57.24
Spar	28.18	42.60
Foam	0.11	0.18

In the second analysis, a chordwise force was assigned as a distributed body force and applied along the chord of the blade from leading edge to trailing edge as shown in Figure 12. An analytical mathematical expression for mean chordwise force was obtained using the forces generated from CAMRAD II for different radial stations as presented in the sixth column of Table A3 in Appendix A. This distribution shows that the force decreases as it approaches the blade tip. Since the blade generates no lift and the forces acting in the chordwise direction are significantly minimized at zero collective, structural loads (out-of-plane and in-plane bending moments), which are the major contributors of structural stress are decreased.

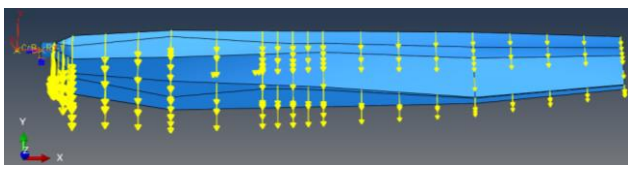

Figure 12. MSH blade model showing force in the chordwise direction.

For this analysis, the peak stress was 74.74GPa also experienced in the skin localized near the blade root. Table 8 breaks down the magnitude of the peak stress experienced in each component. Even though the peak stresses are not as high as those caused by the axial force, the blade experienced stresses that exceed the ultimate stress of both the unidirectional carbon fiber (UTS = ~1.54GPa) and bidirectional carbon fiber (UTS = ~868MPa) in the spar and skin, respectively. This can most likely cause failure in these subcomponents, especially in regions near the blade root due to high stress concentrations.

Table 8. Peak stresses of the blade subjected to a chordwise force.

Blade Component	Peak Stress (GPa) Isotropic	Peak Stress (GPa) Orthotropic
Skin	74.74	127.91
Spar	48.13	95.54
Foam	0.12	0.25

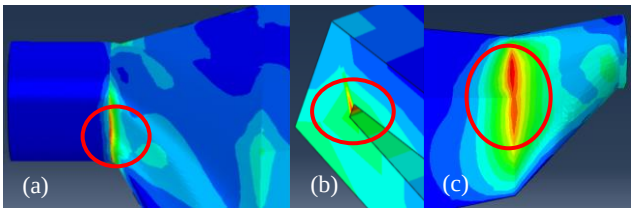

Figure 13. FEA of blade showing regions of peak stress on the (a) skin; (b) spar; and (c) foam due to a chordwise force.

In the third analysis, the normal force was assigned as a distributed body force applied along the blade span in a direction perpendicular to the x-direction according to the global coordinate system defined in (Figure 14). A corresponding analytical mathematical expression was obtained from the mean normal forces generated from CAMRAD II for different radial stations as presented in the seventh column of Table A3 in Appendix A. Based on the analytical mathematical expression, the force distribution oscillated towards the blade tip.

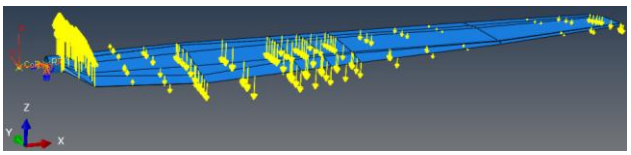

Figure 14. MSH blade model showing normal force assigned along the top surface of the blade.

The blade normal force, comprising the lift and drag forces acting perpendicular to the blade's rotational direction, is a major contributor to the blade's structural loads. At higher RPMs, the magnitude of aerodynamics forces significantly increases due to the airflow velocity, however, at zero

collective, these aerodynamics forces are eliminated, which lowers the structural stresses. Since the largest mean normal force (25.98N) was observed at r/R=0.25, regions in the spar experienced peak stresses as summarized in Table 9. Note that the stresses in the skin, spar, and foam due to the mean normal forces were orders of magnitude lower than the stresses due to mean axial and mean chordwise forces. For this force distribution, the peak stress in the spar was within the allowable limit of the unidirectional carbon fiber (~1.54GPa) defined in the isotropic distribution, but not for the orthotropic distribution. Similarly, the peak stress in the skin was within the allowable limit of the bidirectional carbon fiber (~868MPa) for the isotropic distribution. This implied that a safety factor >1 implied a safer structure with uniform homogeneous carbon fiber distribution. Figure 15 shows the regions near the blade root on the skin, spar, and foam that experienced high stresses.

Table 9. Peak stresses of the blade subcomponents subjected to a normal force.

Blade Component	Peak Stress (MPa) Isotropic	Peak Stress (MPa) Orthotropic
Skin	694.18	1735.90
Spar	1366.90	1860.73
Foam	3.18	7.11

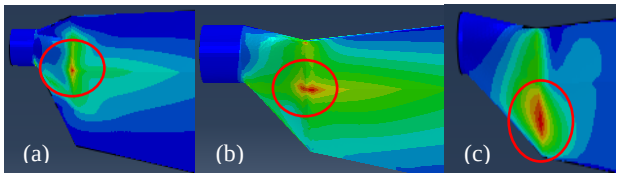

Figure 15. FEA of blade showing regions of peak stress on the (a) skin; (b) spar; and (c) foam due to a normal force.

Finally, the axial, chordwise and normal forces were simulated together (Figure 16) for an ideal case where all forces are exerted on the blade at once. This analysis was compared against the individual cases and to determine how combined forces impacted the blade's overall structural behavior. The results as shown in Table 10, revealed that peak stresses of the blade in this case were relatively close, within a range, to the stresses produced by an axial force (defined as a body force). This demonstrates the dominance of the axial forces also referred to as centrifugal forces, even at zero collective, which induce stresses along the blade span. The orthotropic distribution of the carbon fiber had higher stresses than isotropic distribution. This is due to the non-homogeneous material orientation of the orthotropic properties along the blade span from the root to the tip. Safety factors <1 implied that regions of high stress in the skin and spar based on the ultimate stress of the bidirectional and unidirectional carbon fibers defined respectively are likely to experience failure when exposed to high blade loads.

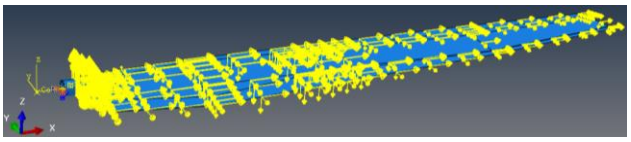

Figure 16. MSH blade model with axial, chordwise, and normal forces assigned along the blade span.

As the blade's RPM varies, higher RPMs will push the blade towards its structural limits due to the significantly magnified centrifugal forces and combinations of increased chordwise and normal forces. As such, it is important to consider proper control systems including pitch control that will likely reduce structural stress by adjusting the blade's angle relative to the airflow.

Table 10. Peak stresses of the blade subcomponents subjected to combined axial, chordwise, and normal forces.

Blade Component	Peak Stress (GPa) Isotropic	Peak Stress (GPa) Orthotropic
Skin	2167.49	3292.06
Spar	911.48	2430.80
Foam	3.10	7.64

NEXT STEPS

Plans for future work to improve the structural integrity of blades with thin airfoils, especially for Mars applications, include adding ply layers as reinforcement, particularly to the blade spar and skin. This will likely increase the blade's stiffness to withstand loads. The structural performance of the blade can also be improved by adjusting the blade geometry, particularly the airfoil shape, chord, and twist along the blade span. Since the blade loads used in the structural analysis are obtained from CAMRAD II, various input parameters for the CAMRAD II simulations including flight conditions, atmospheric conditions, and blade model properties must be considered as they can significantly impact the resulting blade loads and subsequently the blade's structural behavior. Furthermore, blade dynamics analysis involving vibration predictions for complex rotor systems at various rotating speeds can help determine how the blade performance can be improved to minimize failure. Performing torsional analyses will help understand how twisting forces and moments affect the structural integrity of the blade.

CONCLUSIONS

Overall, this work has primarily considered the conceptual MSH blade in a non-rotating state, which precedes rotating analyses of the blade in hover and forward flight. To maintain an optimal lightweight design, unidirectional and bidirectional carbon fiber material properties were used in these analyses. The assumption that the material property distribution in the MSH blade was isotropic and homogeneous was used to determine a baseline distribution; however, an orthotropic material distribution is highly likely for a blade with subcomponents (skin, spar, and foam) and multiple layers of materials in different orientations to ensure reinforcement and structural integrity.

Finite element analysis of the MSH blade as reported in this paper verified the structural performance of the blade under multiple loading conditions. Modal analyses serve as a foundation for complex dynamics and vibrations simulations for complex structures and systems such as transient response analysis or frequency response analysis to predict structural behavior across specific time-varying forces. These analyses ensure that the blade would operate reliably and safely within its operational environment. Factors such as blade twist and pitch can significantly influence the blade's stability and the blade's response to the loads applied. Furthermore, since the blade geometry is relatively nonlinear, it contains abrupt edges. These abrupt sharp edges become regions of stress concentrations with high enough stresses that can potentially lead to blade failure.

For the launch and operational loads analysis, the blade geometry and the material properties proved sufficient since the safety factor (> 1) was within the allowable limit of the materials used for each blade subcomponent. However, for the blade loads analysis, the axial, chordwise, and normal forces generated from CAMRAD II exerted higher forces on the blade, which led to considerably higher stresses that exceeded the allowable limits for each material. This asserts that the carbon fiber material properties may not be sufficient to withstand the loads, though, input parameters and operation conditions such as collective, tip Mach number, and rotor solidity, and blade loading conditions directly impact the blade loads and could alter the blade's overall structural performance. Due to the zero collective setting, aerodynamic loads were significantly reduced and the centrifugal forces dominated, which induced high stresses, particularly in the skin and the spar.

Findings from the structural analysis indicated that the peak stress was prevalent in the blade skin only when the blade was subjected to an axial (centrifugal) force. Otherwise, peak stresses in the spar were observed near the blade root when the blade was subjected to chordwise forces, normal forces, and when all forces were combined. The likelihood of high stress along the blade's length is inevitable with the body forces such as centrifugal forces pulling the blade outwards from its center of rotation. The tension created from this pull affects the blade's shape, which might impact the blade's ability to generate lift depending on the magnitude of the force and may eventually cause failure. The peak stresses experienced in the blade spar exceeded the ultimate stress of the unidirectional carbon fiber (~1.54GPa), making the spar susceptible to failure (FoS<1). The discrepancies between CAMRAD II-based and Abaqus-based results are likely due to the mass, stiffness, and inertial properties generated by BSPGen and utilized by CAMRAD II. The BSPGen tool generates discrete outputs, while Abaqus utilizes a continuous solution. Additionally, the BSPGen tool is actively being refined to generate more accurate results. However, the focus of this work is to express lessons learned, and the discrepancies have allowed for a deeper understanding of how the tools utilized influence results.

Author Contact:
Dr. Dorcas V. Kaweesa, dorcas.kaweesa@nasa.gov
Dr. Gianmarco Sahragard-Monfared,
g.monfared@nasa.gov

ACKNOWLEDGEMENTS

The authors would like to thank the Rotor Test Project for funding this work as well as Mr. Carl Russell and the Aeromechanics Office for the continued support towards rotorcraft tool development for Mars exploration. Special thanks to Mr. Stephen Wright and Mr. Christopher Silva for taking the time to review the manuscript and provide invaluable feedback.

REFERENCES

[1] L. Young and E. W. Aiken., "Vertical Lift Planetary Aerial Vehicles: Three Planetary Bodes and Four Conceptual Design Cases," in *27th European Rotorcraft Forum*, 2001.

[2] B. Pipenberg, W. Keennon, S. A. Langberg and J. D. Tyler, "Development of the Mars Helicopter Rotor System," in *American Helicopter Society 75th Annual Forum*, 2019.

[3] J. Balaram, J. I. Daubar, , J. Bapst and T. Tzanetos, "Helicopters on Mars: Compelling Science of Extreme Terrains Enabled by an Aerial Platform," in *Ninth International Conference on Mars*, 2019.

[4] K. Fujita, H. Karaca and H. Nagai, "Parametric Study of Mars Helicopter for Pit Crater Exploration," in *AIAA 2020-1734. AIAA SciTech 2020 Forum*, 2020.

[5] M. Radotich, S. Withrow–Maser, Z. deSouza, S. Gelhar and H. Gallagher, "A Study of Past, Present, and Future Mars Rotorcraft," in *Vertical Flight Society's 9th Biennial Autonomous VTOL Technical Meeting*, Virtual, January 26-28, 2021.

[6] L. Young, L. Pascal, E. Aiken, G. Briggs, S. Withrow–Maser, G. Pisanich and H. Cummings, "The Future of Rotorcraft and other Aerial Vehicles for Mars Exploration," in *Presented at the Vertical Flight Society's 77th Annual Forum & Technology Display*, Virtual, May 10-14, 2021.

[7] S. Withrow-Maser, Koning W., Kuang W. and W. Johnson, "Recent Efforts Enabling Future Mars Rotorcraft Missions," in *Presented at the VFS Aeromechanics for Advanced Vertical Flight Technical Meeting*, San Jose, CA,, January 21–23, 2020.

[8] S. Withrow–Maser, Johnson W., Young L., H. Cummings, A. Chan, J. Balaram and J. Bapst, "An Advanced Mars Helicopter Design," in *Presented at the AIAA Ascend Conference*, Virtual, November 16–18, 2020.

[9] L. Young, Deluane J., Johnson W., S. Withrow–Maser, H. Cummings, S. E., I. J., A. Schutte, A. Fraeman and R. T. Bhagwat, "Design Considerations for a Mars Highland Helicopter," in *Presented at the AIAA Ascend Conference*, Virtual, November 16-18, 2020.

[10] S. Withrow-Maser, W. Johnson, T. Tzanetos, H. Grip, W. Koning, N. Schatzman, L. Young, A. Chan, A. Ruan, H. Cummings, B. Allan, C. Malpica, L. Meyn, B. Pipenberg and M. Keennon, "Mars Sample Recovery Helicopter: Rotorcraft to Retrieve the First Samples from the Martian Surface," in *Presented at the Vertical Flight Society's 79th Annual Forum & Technology Dsiplay*, West Palm, FL, May 16-19, 2023.

[11] W. Johnson, S. Withrow-Maser, L. Young, C. Malpica, W. J. Koning, W. Kuang, M. Fehler, A. Tuano, A. Chan, A. Datta, C. Chi, R. Lumba, D. Escobar, J. Balaram, T. Tzanetos and H. F. Grip, "Mars Science Helicopter Conceptual Design," NASA/TM—2020–220485, Moffett Field, CA, 2020.

[12] S. Withrow-Maser, W. Johnson, L. Young, W. Koning, W. Kuang, C. Malpica, J. Balaram and T. Tzanetos, "Mars Science Helicopter: Conceptual Design of the Next Generation of Mars Rotorcraft," in *AIAA Ascend Conference*, Virtual, November 16-18, 2020.

[13] H. Grip, L. Jones-Wilson, C. Lefler, A. Duran, B. Inouye, B. Burns, B. Metz, T. Brown, D. Bugby, J. Karras, F. Mier-Hicks, G. Picache, W. Johnson, M. Ueno, G. Sahragard-Monfared and J. Bowman, "The Chopper Next-Generation Mars Rotorcraft: Scaling Ingenuity by a Factor 20," in *2025 IEEE Aerospace Conference*, Big Sky, MT, 2025.

[14] S. Withrow-Maser, W. Johnson, W. Koning, T. Ågren, G. Sahragard-Monfared, J. Bowman, D. Kaweesa, A. Ruan, C. Malpica, L. Jones-Wilson, J. Izraelevitz, J. Delaune, F. Mier-Hicks, K. D. A. Sneeder and M. Veismann, "Critical Aerodynamic and Performance Upgrades to Enable Larger Mars Rotorcraft Such as the Chopper Platform," in *The Vertical Flight Society's 81st Annual Forum & Technology Display*, Virginia Beach, VA, 2025.

[15] R. Singh, "Hexacopter Flight Dynamics on Earth and Martian Surfaces," in *Vertical Flight Society Sixth Decennial Aeromechanics Specialists' Conference*, Santa Clara, CA, February 2024.

[16] R. Lumba, C. Chi, A. Datta, W. Koning, N. Perez Perez and H. Cummings, "Structural Design and Aeromechanical Analysis of Unconventional Blades for Future Mars Rotorcraft," *Journal of the American Helicopter Society*, vol. 68, no. 2, April 2023.

[17] S. Wright, W. Koning, N. Perez Perez, H. Cummings and W. Johnson, "Predicted Performance Effects of Blade Elasticity on Testing of Rotors for Mars," in *Presented at the VFS Autonomous VTOL Technical Meeting*, Mesa, AZ, Jan. 24-26, 2023.

[18] D. Shirazi, A. Chan and W. Johnson, "Rotor Performance Predictions of a Next Generation Mars Science Helicopter," in *Vertical Flight Society Sixth Decennial Aeromechanics Specialists' Conference*, Santa Clara, CA, February 2024.

[19] H. Cummings, N. B. Perez Perez, W. Koning, W. Johnson, L. Young, F. Haddad, E. Romander, J. Balaram, T. Tzanetos, J. Bowman, L. Wagner, S. Withrow-Maser, E. Isaacs, S. Toney, D. Shirazi, S. Conley, B. Pipenberg, A. Datta, R. Lumba, C. Chi, J. K. Smith, C. Cornelius, A. Perez, T. Nonomura and K. Asai, "Overview and Introduction of the Rotor Optimization for the Advancement of Mars eXploration (ROAMX) Project," in *Presented at the VFS Aeromechanics for Advanced Vertical Flight Technical Meeting*, San Jose, CA, January 25-27, 2022.

[20] W. Koning, N. Perez Perez, H. Cummings, E. Romander and W. Johnson, "ELISA: A Tool for Optimization of Rotor Hover Performance at Low

Reynolds Number in the Mars Atmosphere," in *Vertical Flight Society Sixth Decennial Aeromechanics Specialists' Conference*, Santa Clara, CA, February, 2024.

[21] W. Koning, N. Perez Perez, H. Cummings, E. Romander and W. Johnson, "Overview of Rotor Hover Performance Capabilities at Low Reynolds Number for Mars Exploration," in *50th European Rotorcraft Forum*, Marseille, France, 2024.

[22] D. Kaweesa and J. Bowman, "Structural Analysis of Load-Bearing Components in Mars Science Helicopter," in *Presented at the AIAA SciTech Forum*, Orlando, FL, January 6-10, 2025.

[23] C. Chi, R. Lumba, Y. Jung and A. Datta, "Preliminary Structural Design and Aerodynamic Analysis of Mars Science Helicopter Rotors," in *AIAA ASCEND Conference*, 2020.

[24] W. Koning, "Airfoil Selection for Mars Rotor Applications," Technical Report CR—2019–220236, NASA, 2019.

[25] C. Chi, R. Lumba and A. Datta, "Structural Design and Aeromechanical Analysis of the Next Generation Mars Hexacopter Rotor," in *Vertical Flight Society 77th Annual Forum & Technology Display*, Virtual, May 10-14, 2021.

[26] NASA Jet Propulsion Laboratory, "Combination Methods for Deriving Structural Design Loads Considering Vibro-Acoustic, etc., Responses," Preferred Reliability Practices (Practice No. PD-ED-1211), Pasadena, CA..

[27] W. Johnson, "Rotorcraft Aeromechanics Applications of a Comprehensive Analysis," in *HeliJapan 1998: AHS International Meeting on Rotorcraft Technology and Disaster Relief*, Gifu, Japan, April 1998.

[28] H. Cummings, N. Perez, W. Koning and W. Johnson, "Overview and Introduction of the Rotor Optimization for the Advancement of Mars eXploration (ROAMX) Project," in *Aeromechanics for Advanced Vertical Flight Technical Meeting*, 2022.

APPENDIX A

Table A1. Isotropic material properties for blade subcomponents.

Blade Component	Material	Density (kg/m^3)	Spanwise stiffness – MPa (ksi)	Poisson's Ratio
Spar	Unidirectional Carbon Fiber	1522.4	114453 (16600)	0.29
Skin	Bi-Directional Carbon Fiber	1522.4	89631.8 (13000)	0.05
Foam	Rohacell70	75.3	90.3	0.315

Table A2. Orthotropic material properties for blade subcomponents.

Blade Component	Material	Density (kg/m^3)	Spanwise stiffness MPa (ksi)	Transverse stiffness MPa (ksi)	In-Plane Shear stiffness MPa (ksi)
Spar	Unidirectional carbon fiber	1522.4	114453(16600)	6894.8(1000)	4136.85(600)
Skin	Bi-directional carbon fiber	1522.4	89631.8(13000)	89631.8(13000)	4136.85(600)
Foam	Rohacell70	75.3	90.3	90.3	28.4

Table A2-1. Orthotropic Material Properties for Blade Subcomponents.

	Poisson's Ratio		
	nu_{12}	nu_{13}	nu_{23}
Spar	0.29	0.29	0.29
Skin	0.05	0.05	0.05
Foam	0.315	0.315	0.30

Table A3. Blade Forces and Moments Obtained from CAMRAD II Analysis.

Blade Radial Stations (%)	Mean Torsion Moment	Mean Flap Moment	Mean Lag Moment	Mean Axial Force	Mean Chordwise Force	Mean Normal Force
0.1	-0.63	1.10	44.65	2552.68	176.73	9.95
0.2	-0.70	0.91	34.00	2443.99	150.60	20.00
0.25	-0.69	1.14	31.97	2356.48	136.75	25.98
0.3	-0.72	1.11	32.43	2245.99	138.88	17.13
0.45	-0.60	-0.84	19.50	1812.25	92.14	-4.58
0.6	-0.30	-2.06	10.21	1264.83	60.11	12.00
0.75	-0.10	-1.40	4.84	742.48	43.34	18.32
0.9	-0.001	-0.27	0.67	274.33	15.57	9.29
0.95	0.002	-0.06	0.13	117.52	6.60	4.19
1	0	0	0	0	0	0

Nomenclature for MSH Blade Subcomponents

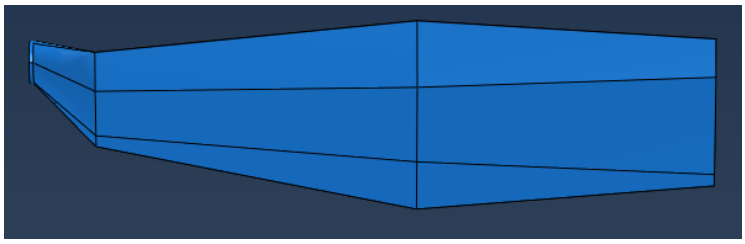

Figure A1. Foam Core.

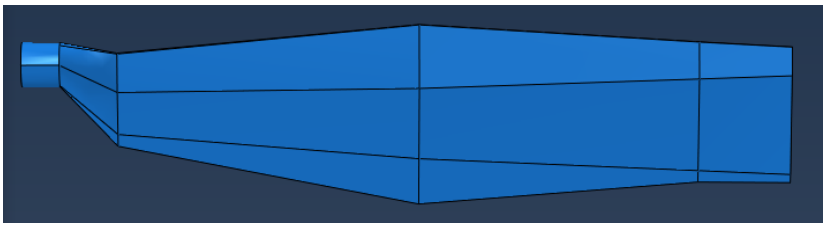

Figure A2. Spar.

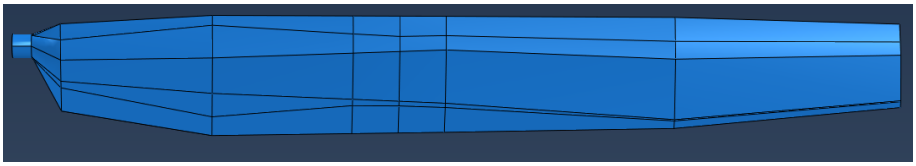

Figure A3. Skin.